Be^{2+}-Induced Red Emission Enhancement in CaAl$_{12}$O$_{19}$:Mn^{4+} for Wide Color Gamut Display: Suppressing Self-Reduction of Mn^{4+} to Mn^{2+}

Liwen Zheng, Liangliang Zhang,* Limin Fang, Hao Wu, Huajun Wu, Guo-Hui Pan, Yuxin Yang, Yongshi Luo, Zhendong Hao, and Jiahua Zhang*

Mn^{4+}-activated CaAl$_{12}$O$_{19}$ (CAO: Mn^{4+}) is recognized as a promising candidate for red phosphor used in wide color gamut displays. However, the spontaneous self-reduction of Mn^{4+} to Mn^{2+} occurs for charge compensation through Mn^{2+}-Mn^{4+} substitution for Al^{3+}-Al^{3+}, lowering the quantum efficiency of Mn^{4+}. To suppress the self-reduction, some divalent metal ions, including Ba^{2+}, Sr^{2+}, Cd^{2+}, Zn^{2+}, and Mg^{2+}, are added for charge compensation instead of Mn^{2+}, but only small luminescence enhancement is observed. In this paper, remarkable luminescence enhancement in CAO: Mn^{4+} via co-doping Be^{2+} is reported. The photoluminescence properties are studied as a function of Be^{2+} doping concentration, and the optimal Be^{2+} concentration of 0.01 is found. The internal quantum efficiency of 74.9% and external quantum efficiency of 56.3% are achieved under UV excitation, higher than those via co-doping other divalent metal ions. This study indicates that the addition of Be^{2+} dominates the charge compensation because Be^{2+} is closer to Al^{3+} in size than Mn^{2+} and other divalent metal ions. The backlight light-emitting diodes using CAO: Mn^{4+}, Be^{2+} are fabricated, exhibiting a 110.1% Nation Television Standards Committee (NTSC) color gamut, wider than both the current commercial backlight using K$_2$SiF$_6$: Mn^{4+} (KSF) red phosphor and the conventional one using YAG yellow phosphor.

1. Introduction

Phosphor-converted light emitting diodes (Pc-LEDs) have shown great benefits in daily lighting, plant growth, phototherapy, and nondestructive testing due to their easy portability and high energy efficiency.[1–6] Pc-LEDs also show attractive application prospects in high-color gamut display that needs narrow-emitting phosphors.[5–7] Mn^{4+} is often selected for red narrow-emitting phosphor due to its $^2E_g \rightarrow {}^4A_{2g}$ transition, such as the commercial K$_2$SiF$_6$: Mn^{4+} (KSF) red phosphor. Due to its high efficiency and narrow band, KSF has received lots of attention.[8–10] However, the preparation of efficient KSF requires the use of HF, which is not environmentally friendly. In addition, the chemical stability of KSF is poor with a decomposition temperature of 150 °C. In a humid environment, Mn^{4+} is also prone to deliquescence to Mn^{3+}, such as KMnF$_4$·H$_2$O and K$_2$MnF$_5$·H$_2$O, which competes with Mn^{4+} for absorption and reduces the phosphor quantum efficiency.[11–13] Luckily, oxides have excellent chemical stabilities and can be easily prepared by conventional high-temperature solid reactions. However, Mn^{4+} in oxides mostly exhibits deep red emission, which is insensitive to the human eyes and unsuitable for displays.[14–20] Therefore, it is still a challenge to prepare efficient and chemically stable narrow-emitting-red phosphors.

CaAl$_{12}$O$_{19}$: Mn^{4+} (CAO: Mn^{4+}) is a promising material because of its excellent chemical stability, extremely high zero phonon emission, narrow full width at half maximum (FWHM), and high quantum efficiency.[21–29] To enhance its efficiency, a lot of work has been done: Murata et al. enhanced the crystallinity of the sample by flux CaF$_2$ to improve the luminescence intensity.[30] Wu et al. reduced the nonradiative path by mixing CAO: Mn^{4+} with MgAl$_2$O$_4$ in a solid solution to improve the luminescence intensity.[31] Zheng et al. introduced mixed-phase emission peaks by replacing Ca^{2+}-Al^{3+} with Y^{3+}-Mg^{2+} to improve the quantum efficiency.[32] Zhao and He et al. improved the quantum efficiency by co-doping Zn^{2+} to balance the charge.[33,34] Zhang et al. enhanced the luminescence by doping Mg^{2+} to prevent the concentration quenching

L. Zheng, L. Zhang, L. Fang, H. Wu, H. Wu, G.-H. Pan, Y. Yang, Y. Luo, Z. Hao, J. Zhang
State Key Laboratory of Luminescence and Applications
Changchun Institute of Optics
Fine Mechanics and Physics
Chinese Academy of Sciences
Changchun 130033, China
E-mail: zhangliangliang@ciomp.ac.cn; zhangjh@ciomp.ac.cn
L. Zheng, Y. Yang, J. Zhang
Center of Materials Science and Optoelectronics Engineering
University of Chinese Academy of Sciences
Beijing 100049, China
L. Fang
School of Materials Science and Engineering
Changchun University of Science and Technology
Changchun 130022, China

**ADVANCED
SCIENCE NEWS**

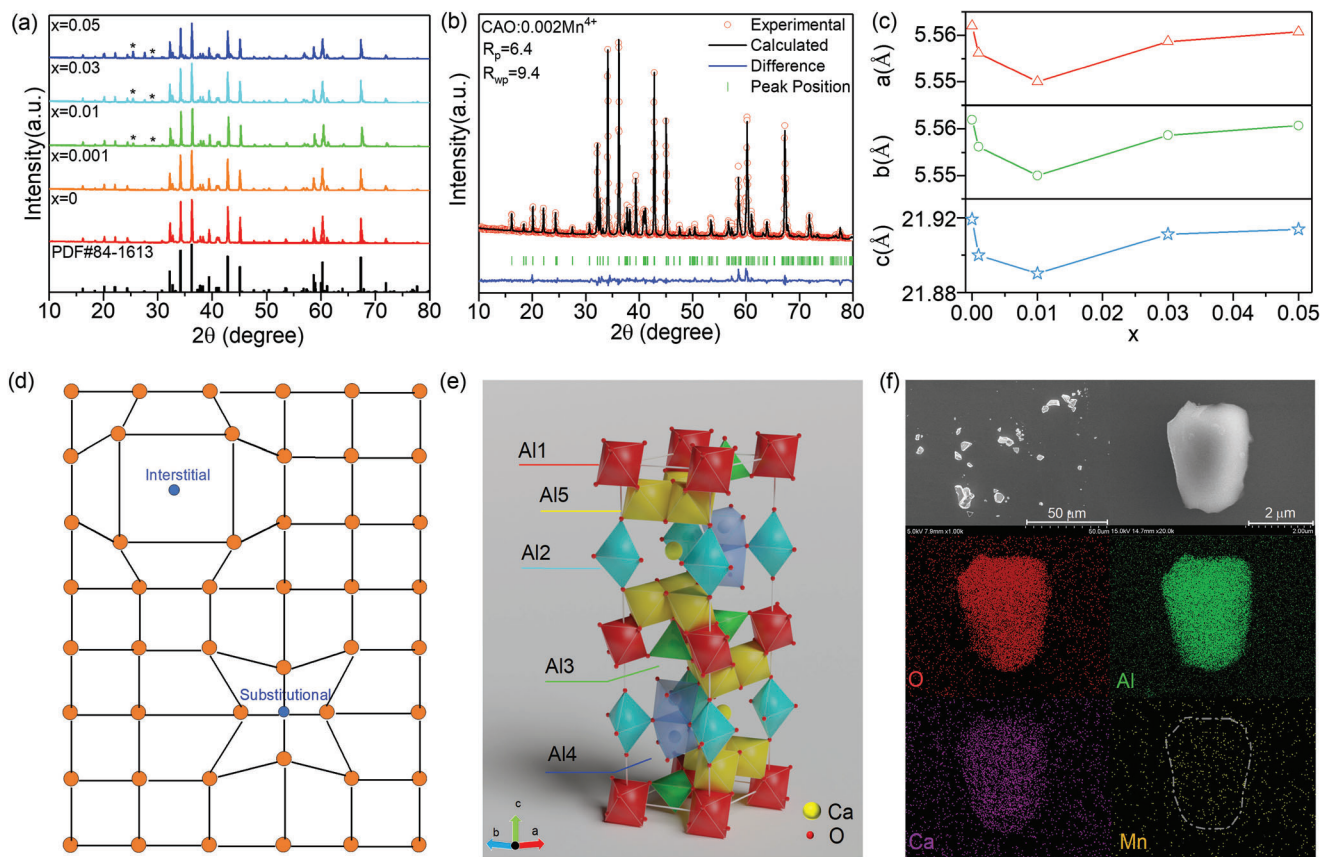www.advancedsciencenews.com

**ADVANCED
OPTICAL
MATERIALS**

www.advopticalmat.de

Figure 1. a) XRD patterns of CAO: $0.002Mn^{4+}$, xBe^{2+}, * stands for $CaAl_4O_7$. b) Rietveld refinement XRD pattern of CAO: $0.002Mn^{4+}$. c) Variation of lattice parameters for CAO: $0.002Mn^{4+}$, xBe^{2+}. d) Schematic diagram of two Be^{2+} substitutional modes. e) Schematic diagram of the primitive cell structure of CAO. f) SEM and corresponding elemental mapping images for CAO: $0.002Mn^{4+}$, $0.01Be^{2+}$.

of Mn^{4+}.[35] However, the quantum efficiency still needs to be improved.

In this paper, we report the realization of significant luminescence enhancement of CAO: Mn^{4+} by co-doping Be^{2+}. The mechanism of luminescence enhancement is studied. The replacement of Be^{2+}-Mn^{4+} pairs to Al^{3+}-Al^{3+} pairs is proposed. Such a replacement will compensate for the charge and suppress the self-reduction of Mn^{4+} to Mn^{2+}, which can be demonstrated in the spectra by comparing the content of Mn^{4+} and Mn^{2+} in CAO: Mn^{4+}, Be^{2+}. In addition, we systematically discuss all common divalent metal ions and compare their impact on emission spectra. It is found that Be^{2+} is closer to Al^{3+} in size than Mn^{2+} and other divalent metal ions, resulting in the strongest charge compensation and luminescence enhancement. This phenomenon can provide a new method to increase the luminescence intensity of Mn^{4+}.

2. Results and Discussion

2.1. Structural Characterization

X-ray diffraction (XRD) patterns of CAO: $0.002Mn^{4+}$, xBe^{2+} (x = 0, 0.001, 0.01, 0.03, 0.05) samples match well with the international standard card $CaAl_{12}O_{19}$ (PDF#84-1613), except for the

small impurity peaks from $CaAl_4O_7$ (**Figure 1**a,b and Figure S1, Supporting Information). We believe that a small number of impurities will not affect our results. As shown in Figure 1c, the lattice constants increase and then decrease as Be^{2+} concentration increases. This can be explained by two substitution modes of Be^{2+} as shown in Figure 1d. Generally, Be^{2+} (r = 0.45 Å, CN = 6) tends to replace Al^{3+} (r = 0.53 Å, CN = 6) with small radius difference. These substitutional Be^{2+} ions cause lattice contraction. However, the lattice constants start to rise while x over 0.01, caused by interstitial Be^{2+}.[36] In other words, two substitution modes of Be^{2+} are in competition, with interstitial Be^{2+} dominating when x is over 0.01 and substitutional Be^{2+} dominating when x is under 0.01. The crystal structure of CAO with the space group $P6_3/mmc$ is shown in Figure 1e. CAO has a magnetite structure with five lattice sites for Al^{3+} ions. Al1, Al4, and Al5 form a sixfold coordinated octahedron, respectively, while Al2 displays a fivefold coordinated bipyramid. Al3 and four oxygen ions combine to create a tetrahedron. It is well known that Mn^{4+} ions prefer to occupy octahedral sites due to the electronic configuration of $3d^3$, so any of the Al1, Al4, and Al5 sites may be occupied. The calculation of Musashi et al. shows that Mn^{4+} preferentially occupies Al4 sites among these three sites since its relative total electronic energy is 0.[37] Scanning electron microscope (SEM) and corresponding elemental mapping images for CAO: $0.002Mn^{4+}$, $0.01Be^{2+}$ are shown in Figure 1f with an irregular morphology and

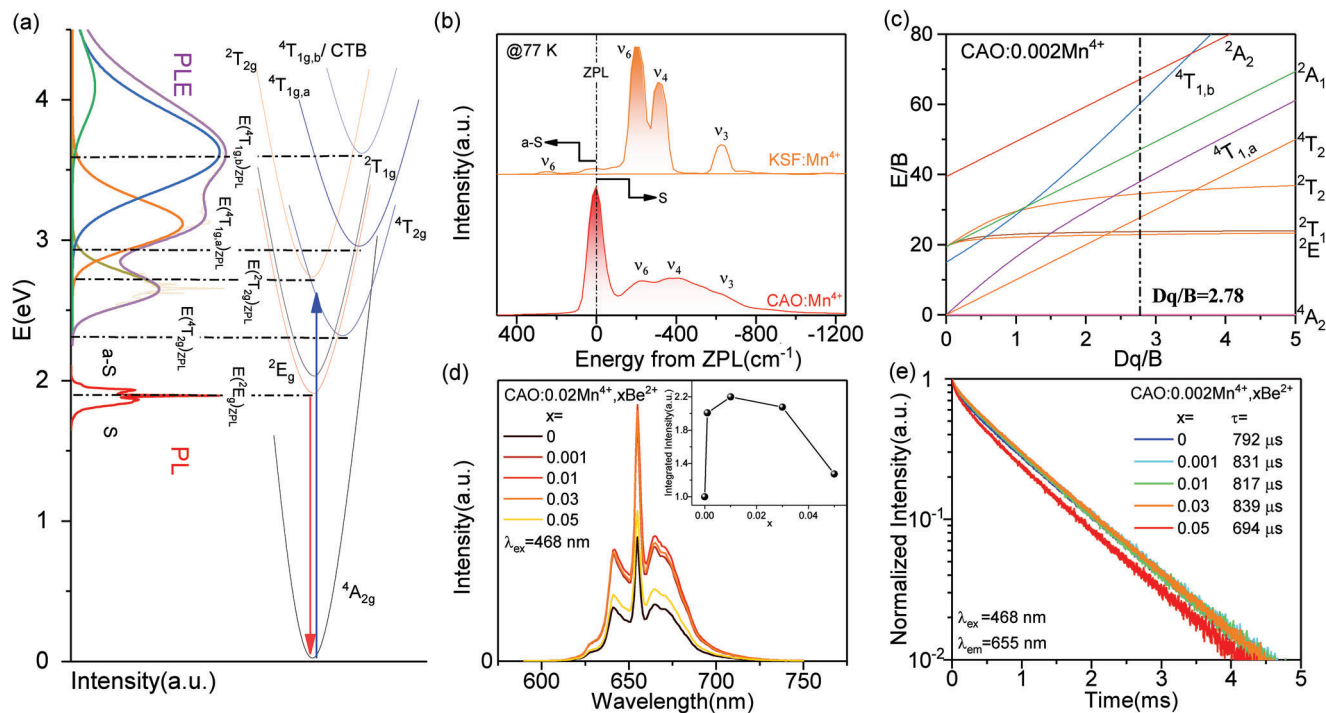**Figure 2.** a) PL and PLE spectra of CAO: $0.002Mn^{4+}$ (left), the configuration coordinate diagram of Mn^{4+} in CAO host (right). b) Comparison of the vibronic emissions of CAO: $0.002Mn^{4+}$ and KSF: Mn^{4+} at 77 K. c) Tanabe–Sugano diagram of CAO: $0.002Mn^{4+}$. d) PL spectra of CAO: $0.002Mn^{4+}$, xBe^{2+}. e) Fluorescence decay curves of CAO: $0.002Mn^{4+}$, xBe^{2+}.

homogeneous distribution of Mn, Ca, Al, O elements (see energy dispersive spectrometer [EDS] spectrum in Figure S2, Supporting Information).

2.2. Addition of Be2+ Induced Luminescence Enhancement

The fluorescence spectra and configuration coordinate diagram of CAO: $0.002Mn^{4+}$ are shown in **Figure 2**a. The photoluminescence excitation (PLE) spectrum of the sample has four major broadband excitation peaks located at 2.64 (468 nm), 3.11 (398 nm), 3.63 (341 nm), and 4.03 eV (307 nm), corresponding to Mn^{4+} characteristic transitions of $^4A_{2g} \rightarrow {}^4T_{2g}$, $^4A_{2g} \rightarrow {}^2T_{2g}$, $^4A_{2g} \rightarrow {}^4T_{1g,a}$ and $^4A_{2g} \rightarrow {}^4T_{1g,b}$/charge transfer band (CTB), respectively. In contrast to the PLE spectrum, the photoluminescence (PL) spectrum shows a narrow-line-emission peak located at 1.89 eV (655 nm) due to the spin and parity forbidden transition of ^2E_g to $^4A_{2g}$. The sidebands on each side of 655 nm come from the Stokes (S) and anti-Stokes (a-S) vibronic emissions originating from three PL-active phonons provided in Figure 2b. Group theory states that octahedral with an O_h point group, such as $[MnO_6]$ and $[MnF_6]$, have six kinds of vibrations, and three of them, called ν_3 (T_{1u}), ν_4 (T_{1u}), and ν_6 (T_{2u}), are PL-active. The coupling of $^2E_g \rightarrow {}^4A_{2g}$ with these three vibrational modes will release the parity selection rule and realize the energy level transition.[38,39] To better illustrate these three modes in CAO: Mn^{4+}, it is compared to the well-known KSF: Mn^{4+}. With the zero phonon line (ZPL) setting as zero point, the energy differences between ZPL and the emission peaks correspond to three vibrational modes with $\nu_6 = 228$ cm^{-1}, $\nu_4 = 365$ cm^{-1}, and $\nu_3 =$

632 cm^{-1}. The crystal field parameters were also calculated by the following equations to accurately depict the environment of Mn^{4+}.

$$E\left({}^4T_{2g}\right) = 10Dq \tag{1}$$

$$\frac{B}{Dq} = \frac{\left(\frac{\Delta E}{Dq}\right)^2 - 10\left(\frac{\Delta E}{Dq}\right)}{15\left(\frac{\Delta E}{Dq} - 8\right)} \tag{2}$$

$$\frac{E\left({}^2E_g\right)}{B} = \frac{3.05C}{B} + 7.9 - \frac{1.8B}{Dq} \tag{3}$$

where $E({}^4T_{2g})$ and $E({}^2E_g)$ are the energy of $^4T_{2g}$ and ^2E_g. Dq is the crystal field strength. ΔE is the energy difference between $^4T_{1g,a}$ and $^4T_{2g}$. B and C are two Racah parameters with $B = 766$ cm^{-1} and $C = 3181$ cm^{-1}. A strong crystal field is found with $Dq/B = 2.78$ (>2.1). The parameters above are reliable since they are in good agreement with Equation (4) fitted by Adachi.[40]

$$E\left({}^2E_g\right) = 0.0027B - 0.030 \, eV \tag{4}$$

The parameter β_1 was calculated using Equation (5) to quantitatively describe the nephelauxetic effect in the spectroscopy of the Mn^{4+}.

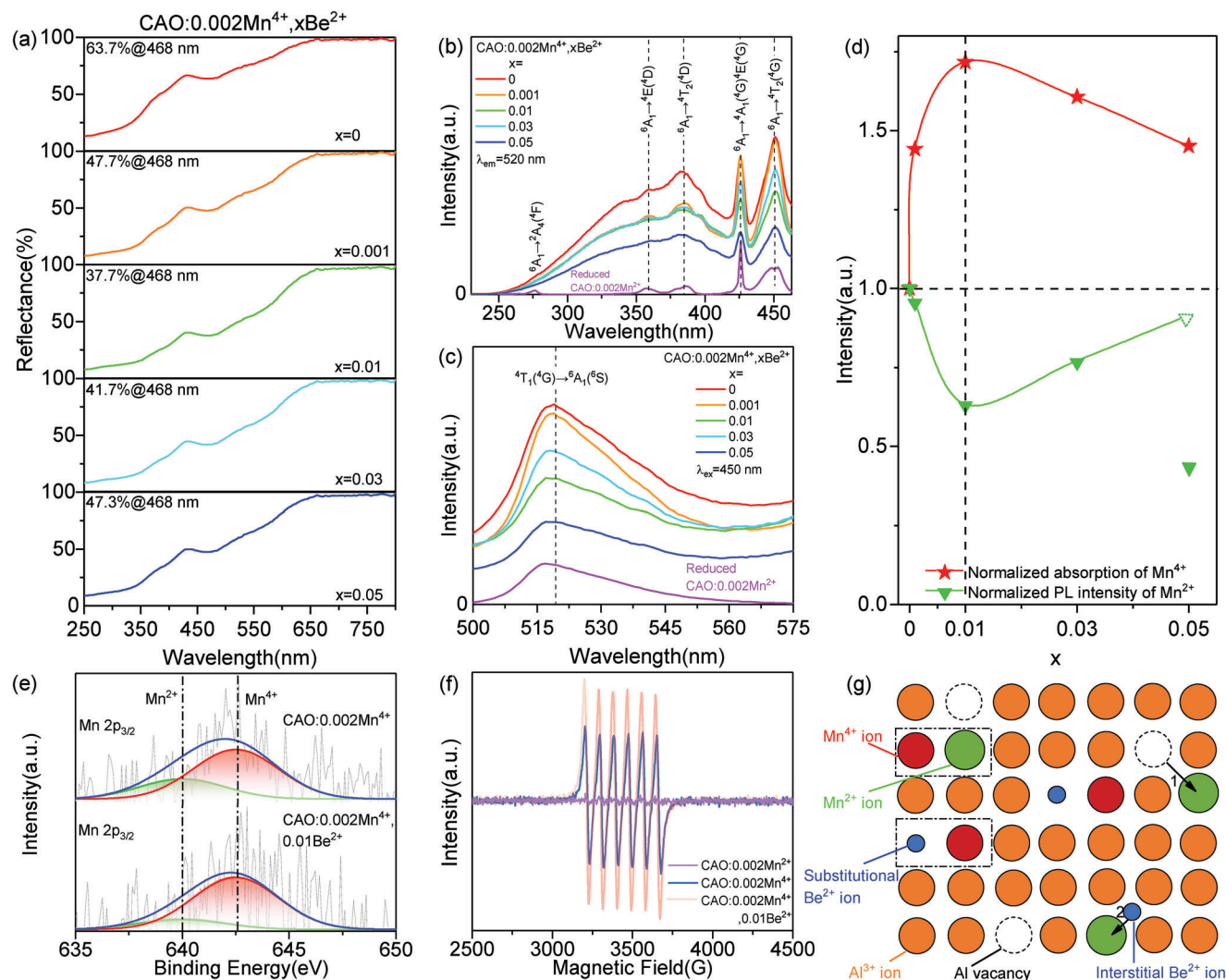$$\beta_1 = \sqrt{\left(\frac{B}{B_0}\right)^2 + \left(\frac{C}{C_0}\right)^2} \tag{5}$$

Figure 3. a) Diffuse reflectance spectra of CAO: $0.002Mn^{4+}$, xBe^{2+}. b) PLE spectra of Mn^{2+} in CAO: $0.002Mn^{4+}$, xBe^{2+}. c) PL spectra of Mn^{2+} in CAO: $0.002Mn^{4+}$, xBe^{2+}. d) Content of Mn^{4+} and Mn^{2+}, the dotted triangle represents the possible Mn^{2+} emission intensity without quenching. e) XPS spectra of Mn $2p_{3/2}$. f) EPR signals. g) Diagram of the mechanism of Be^{2+} action.

Here B_0 and C_0 are the Racah parameters of free Mn^{4+} with 1160 and 4303 cm^{-1}, respectively. β_1 is calculated to 0.99 which is also a trustworthy value because it agrees well with Equation (6) fitted by Brik et al.[41]

$$E\left(^2E_g\right) = -142.83 + 15544.022\beta_1 \qquad (6)$$

It is shown in Figure 2d that the addition of Be^{2+} could significantly enhance the PL intensity of CAO:$0.002Mn^{4+}$ (see Figure S3, Supporting Information, for more spectra information). The integrated intensity increases and then decreases with the increase of Be^{2+} concentration in Figure 2d inset. The optimal η_{IQE} and η_{EQE} of CAO:$0.002Mn^{4+}$, $0.01Be^{2+}$ are shown in Figure S4 and Tables S1 and S2, Supporting Information, with η_{IQE} of 74.9% and η_{EQE} of 56.3% at 360 nm excitation. These are the highest values reported so far via co-doping divalent ions: Zhang et al. co-doped Mg^{2+} (η_{IQE} = 56.1%, λ_{ex} = 340 nm).[35] Zheng et al. co-doped Mg^{2+}, Y^{3+} (η_{IQE} = 65%, λ_{ex} = 320 nm).[32]

and Zhao et al. co-doped Zn^{2+} (η_{IQE} = 67%, λ_{ex} = 360 nm).[33] However, the lifetime of ^2E_g does not significantly change with the addition of Be^{2+}, which means that the emission efficiency of ^2E_g does not change except $x = 0.05$ possibly caused by internal defects as shown in Figure 2e.

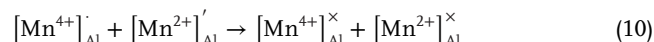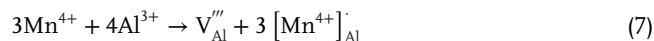## 2.3. Be^{2+} Manipulated Mn^{4+} and Mn^{2+} Numbers

The diffuse reflection spectra of CAO: $0.002Mn^{4+}$, xBe^{2+} are shown in **Figure 3**a. Besides the CAO host absorption at 250 nm (Figure S5, Supporting Information) the absorption bands at 350 and 468 nm originated from the unique Mn^{4+} absorption as compared with the PLE spectra of Mn^{4+} (Figure S3c, Supporting Information) and are normally proportional to the concentration of Mn^{4+}. It is found that Mn^{4+} absorption increases with the increase of Be^{2+} concentration up to 0.01, which means that Be^{2+} can increase Mn^{4+} concentration.

**ADVANCED
SCIENCE NEWS**

www.advancedsciencenews.com

**ADVANCED
OPTICAL
MATERIALS**

www.advopticalmat.de

Figure 3b shows the PLE spectra of CAO: $0.002Mn^{4+}$, xBe^{2+} monitored at 520 nm which is the peak wavelength of Mn^{2+} emission (Figure 3c). PLE spectra consist of a broad band covering a 300–400 nm UV region with four sharp peaks located at 359, 385, 426, and 450 nm. The four PLE peaks are evident in the PLE spectrum of CAO:$0.002Mn^{2+}$ shown at the bottom of Figure 3b and are assigned to Mn^{2+} $^6A_1 \to ^4E(^4D)$, $^6A_1 \to ^4T_2(^4D)$, $^6A_1 \to ^4A_1(^4G)^4E(^4G)$, and $^6A_1 \to ^4T_2(^4G)$, respectively. This means that there are some Mn^{2+} in CAO: $0.002Mn^{4+}$, xBe^{2+}. The broad PLE band is attributed to Mn^{4+} (Figure S3c, Supporting Information). The appearance of the Mn^{4+} PLE band for monitoring at 520 nm is due to the stray light of the strong Mn^{4+} emission. One can see that the PLE peak of Mn^{2+} at 450 nm exhibits a trend of decrease and then increase as Be^{2+} concentration increases, closely matching the trend of increase and then decrease for Mn^{4+} absorption shown in Figure 3a. This reflects the variation of Mn^{2+} and Mn^{4+} numbers with Be^{2+} concentration. Figure 3d shows the comparison of Mn^{4+} absorption intensity and Mn^{2+} emission intensity as a function of Be^{2+} concentration. One can see that with Be^{2+} ($x < 0.01$) increasing, the amount of Mn^{4+} grows while Mn^{2+} declines, indicating the suppression of Mn^{4+} to Mn^{2+} self-reduction. However, Mn^{4+} intensity starts to decline for $x > 0.01$, which will be discussed later.

To further prove the conversion between Mn^{4+} and Mn^{2+}, X-ray photoelectron spectroscopy (XPS) and electron paramagnetic resonance (EPR) are also measured in CAO: $0.002Mn^{4+}$ and CAO: $0.002Mn^{4+}$, $0.01Be^{2+}$ and depicted in Figure 3e,f. The XPS spectra of Ca, Al, and O are almost identical (Figure S6, Supporting Information), while those of Mn show different features (Figure 3e). According to the previous reports,[42,43] the $2p_{3/2}$ spectra of Mn can be decomposed into peaks of Mn^{2+} at 640 eV and Mn^{4+} at 642 eV. It is apparent that (Figure 3e) the addition of Be^{2+} enables a high content of Mn^{4+} and a low content of Mn^{2+}. EPR is also used to prove the valence state of Mn as shown in Figure 3f. The six typical hyperfine peaks come from the M_S transition $-1/2 \to +1/2$ of Mn^{4+}, whose unpaired electrons interact with the Mn nucleus (nucleus spin $I = 5/2$) and the g factor is about 2.00.[44–48] The sample with the addition of Be^{2+} has stronger signals of Mn^{4+} compared with the Be^{2+}-free sample. It should be noted that the EPR signals could not originate from Mn^{2+} because no EPR signal is detected in Mn^{2+} doped CAO, as shown in Figure 3f. In summary, all the evidence indicates that the addition of Be^{2+} can suppress the self-reduction of Mn^{4+} to Mn^{2+}.

Figure 3g illustrates the diagram of the mechanism of Be^{2+}-induced suppression of self-reduction of Mn^{4+} to Mn^{2+}. Mn^{2+} comes from the self-reduction of Mn^{4+} because MnO_2 is used as the manganese source and reacts in air in this work. According to the previous theories of Su et al.,[49,50] the doping of Mn^{4+} into CAO is an aliovalent replacement of Al^{3+}. Four Al^{3+} will be replaced by three Mn^{4+} for charge balance. As a result, three positive defects $[Mn^{4+}]_{Al}^{\cdot}$ and one vacancy defect of V_{Al}''' with three negative charges are created for every three Mn^{4+} replacements. Vacancy defect of V_{Al}''' will serve as a donor of electrons, while $[Mn^{4+}]_{Al}^{\cdot}$ will serve as an acceptor of electrons. At high temperatures, the electrons are liberated from V_{Al}''' and captured by $[Mn^{4+}]_{Al}^{\cdot}$ into the 3d orbital leading to partial reduction of Mn^{4+} to Mn^{2+} as shown in Figure 3g process 1. Eventually, one Mn^{4+}

with one Mn^{2+} charge balances out two Al^{3+}. The above processes could be expressed as follows

$$3Mn^{4+} + 4Al^{3+} \to V_{Al}''' + 3\left[Mn^{4+}\right]_{Al}^{\cdot} \tag{7}$$

$$V_{Al}''' \to V_{Al}^{\times} + 3e^- \tag{8}$$

$$\left[Mn^{4+}\right]_{Al}^{\cdot} + 2e^- \to \left[Mn^{2+}\right]_{Al}' \tag{9}$$

$$\left[Mn^{4+}\right]_{Al}^{\cdot} + \left[Mn^{2+}\right]_{Al}' \to \left[Mn^{4+}\right]_{Al}^{\times} + \left[Mn^{2+}\right]_{Al}^{\times} \tag{10}$$

Al^{3+} can be none equivalently replaced by Be^{2+} in CAO. A negatively charged defect $[Be^{2+}]_{Al}'$ produced by this replacement can react with $[Mn^{4+}]_{Al}^{\cdot}$ to create a charge balance. Such a reaction of Be^{2+}-Mn^{4+} pairs can effectively replace the Al^{3+}-Al^{3+} pairs and increase Mn^{4+} content as shown in the dotted boxes of Figure 3g. The following equation can be used to explain the process

$$\left[Be^{2+}\right]_{Al}' + \left[Mn^{4+}\right]_{Al}^{\cdot} \to \left[Be^{2+}\right]_{Al}^{\times} + \left[Mn^{4+}\right]_{Al}^{\times} \tag{11}$$
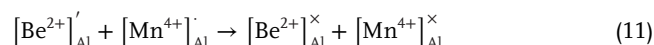
However, Be^{2+} is also likely to become an interstitial impurity because of its small radius, which is supported by the observed increase in lattice constants for $x > 0.01$, as shown in Figure 1c. According to the results obtained by Xu et al.,[51] these interstitial ions become the donors of electrons thus enhancing the self-reduction and increasing Mn^{2+} content as indicated in process 2 in Figure 3g. As a result, two types of Be^{2+} control the Mn^{4+} concentration. When x is less than 0.01, substitutional Be^{2+} will predominate and self-reduction of Mn^{4+} to Mn^{2+} is suppressed. When x is greater than 0.01, the interstitial Be^{2+} becomes important and the self-reduction suppression is partially relieved.

2.4. Effect of Other Divalent Metal Ions on Emission Intensity

The divalent Be^{2+} can effectively compensate for the charge while not all the divalent ions can. **Figure 4**a shows the emission spectra corresponding to different divalent ion Re^{2+} doping with the same concentration. It is found that the shape of emission peaks did not change while their intensity gradually increases as the radius of co-doping divalent metal ions decreases: Ba^{2+} ($r = 1.35$ Å, CN = 6), Sr^{2+} ($r = 1.18$ Å, CN = 6), Ca^{2+} ($r = 1$ Å, CN = 6), Cd^{2+} ($r = 0.95$ Å, CN = 6), Zn^{2+} ($r = 0.74$ Å, CN = 6), Mg^{2+} ($r = 0.72$ Å, CN = 6), and Be^{2+} ($r = 0.45$ Å, CN = 6).[52] The intensity changes independently with the emission efficiency of ^2E_g and thermal stability (see Figures S7 and S8, Supporting Information). Figure 4b shows the relative integrated intensities for doping different divalent metal ions with Ca^{2+} setting as a reference point. It is found that the small ions such as Cd^{2+}, Zn^{2+}, Mg^{2+}, and Be^{2+} exhibit luminescence enhancement while Ba^{2+} and Sr^{2+} of big ions result in luminescence decrease. This phenomenon can be well explained by the ability of substitution of Al^{3+}. Compared to Mn^{2+} ($r = 0.67$ Å, CN = 6), Be^{2+} is closer to Al^{3+} ($r = 0.53$ Å, CN = 6) in size and has the advantage of replacing Al^{3+}. This is why Be^{2+} can effectively suppress the self-reduction of Mn^{4+} to Mn^{2+} and give rise to remarkable luminescence enhancement. However, other divalent metal ions have larger radii than Mn^{2+} and hardly replace Al^{3+}. As a result, other divalent metal ions result in small luminescence enhancement. Alternatively, the divalent
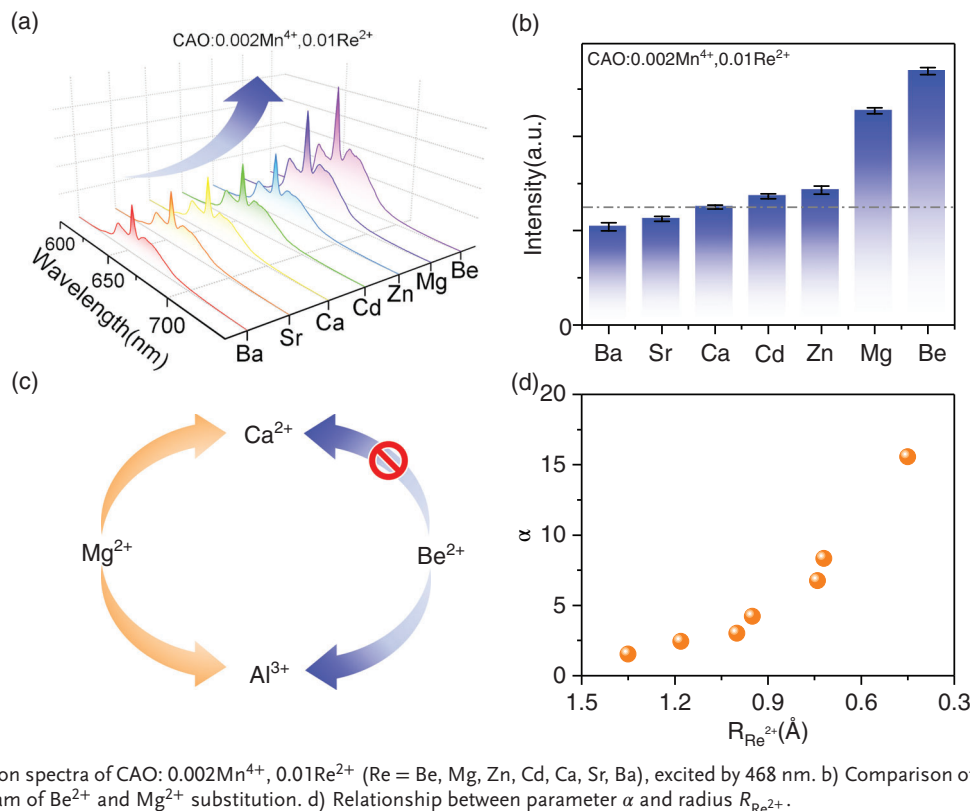
Figure 4. a) Emission spectra of CAO: $0.002Mn^{4+}$, $0.01Re^{2+}$ (Re = Be, Mg, Zn, Cd, Ca, Sr, Ba), excited by 468 nm. b) Comparison of integrated intensity. c) Schematic diagram of Be^{2+} and Mg^{2+} substitution. d) Relationship between parameter α and radius $R_{Re^{2+}}$.

metal ions can replace Ca^{2+} without charge mismatch[25,26,31,32,35] as shown in Figure 4c. The following equation gives the parameter α, which could describe the choice of replacing Al^{3+} and Ca^{2+}

$$\alpha = \frac{1 - \left(R_{Re^{2+}} - R_{Al^{3+}} \right) / R_{Al^{3+}}}{1 - \left(R_{Re^{2+}} - R_{Ca^{2+}} \right) / R_{Ca^{2+}}} \qquad (12)$$

where $R_{Re^{2+}}$, $R_{Al^{3+}}$, and $R_{Ca^{2+}}$ are the radii of divalent metal ions, Al^{3+} and Ca^{2+}, respectively. The fraction represents the ability to replace Al^{3+} with divalent metal ions and the denominator represents the ability to replace Ca^{2+} by the divalent metal ions. The parameter α with the same trend of Figure 4b reflects the competition between the above two replacements, as shown in Figure 4d. Be^{2+} is closer to Al^{3+} in size and has a stronger ability to replace Al^{3+} for charge compensation and luminescence enhancement. It is worth mentioning that Cd (1.69) and Zn (1.65) have larger electronegativity than Be (1.57) and are more conducive to charge compensation of Mn^{4+}. However, their larger radii make them difficult to replace Al^{3+}. In other words, the radius of the divalent ions dominates the luminescence enhancement. This conclusion is further supported by the realization of Be^{2+} induced remarkable luminescence enhancement in Mn^{4+}-doped other type aluminates $YAlO_3$: Mn^{4+}, $LaAlO_3$: Mn^{4+}, and $GdAlO_3$: Mn^{4+} (shown in Figure S9, Supporting Information). Figures S10 and S11, Supporting Information, show the water resistance and photostability of CAO: Mn^{4+} and KSF: Mn^{4+}.

2.5. Application in LED Backlight Source for LCD

As shown in **Figure 5**a, the LCD is mainly composed of the LCD module and the backlight module. The backlight module consists of a light guide plate, a reflector, and LEDs (a more detailed structure is not shown because it is not the focus of this work). In this paper, LEDs using CAO: Mn^{4+}, Be^{2+} are prepared and compared with the conventional LEDs using YAG as shown in Figure 5b. It is found that the addition of CAO: Mn^{4+}, Be^{2+} allows LEDs to have a strong red lighting performance. To compare the color gamut of these LEDs, the CIE color coordinates and Nation Television Standards Committee (NTSC) are shown in Figure 5c. The color gamut of the conventional LED using YAG (black dashed line) is calculated as 68.6% of NTSC and the commercial LED using KSF (yellow dashed triangle) is calculated as 102.5% of NTSC. In this work, 110.1% of NTSC is obtained and the color coordinate of CAO: Mn^{4+}, Be^{2+} is (0.7199, 0.2801). Compared with LEDs using YAG, LEDs using CAO: Mn^{4+}, Be^{2+} gain a larger color gamut because of the increased red component. It is worth noting that the color gamut is only calculated by the phosphors' spectra, and the effects of color filters are not taken into consideration. Liquid crystal displays based on LEDs using CAO: Mn^{4+}, Be^{2+} and conventional LEDs using YAG are shown in Figure 5d. The photos above are from backlight LEDs using CAO: Mn^{4+}, Be^{2+} while the photos below are from backlight LEDs using YAG. The photos above show a more vibrant color compared with the ones below.
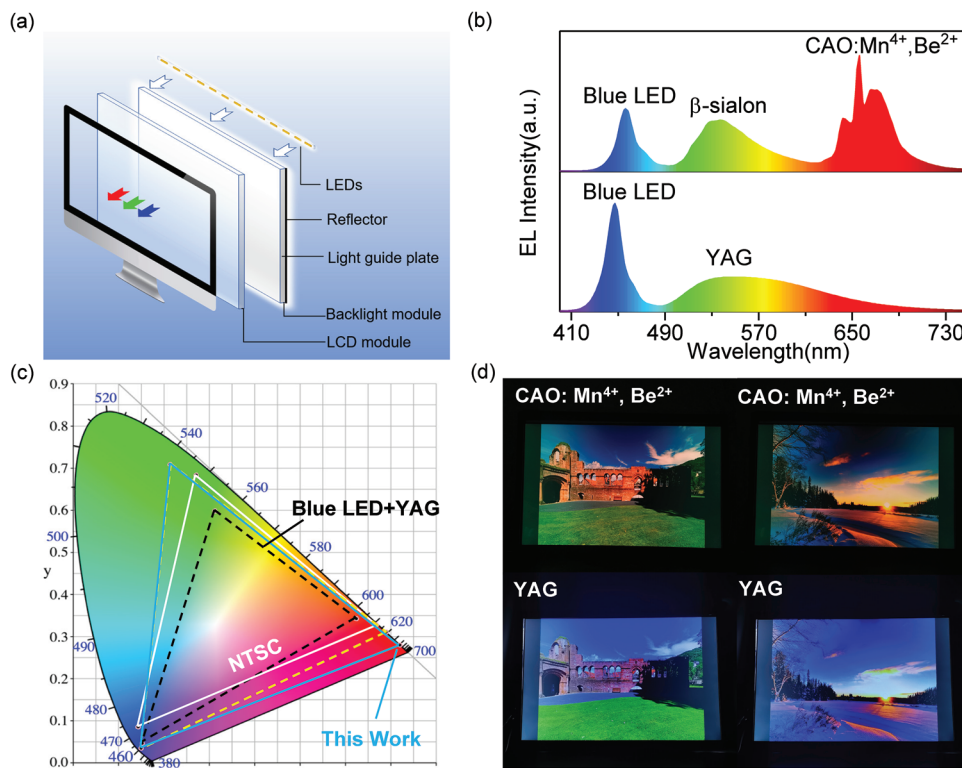
**ADVANCED
SCIENCE NEWS**

www.advancedsciencenews.com

**ADVANCED
OPTICAL
MATERIALS**

www.advopticalmat.de

Figure 5. a) Structure diagram of the LCD. b) EL spectra of LED using CAO: Mn^{4+}, Be^{2+} and conventional LED using YAG. c) CIE color coordinates of LED using CAO: Mn^{4+}, Be^{2+} (blue solid triangle), conventional LED using YAG (black dashed triangle), commercial LED using KSF (yellow dashed triangle), and NTSC standard (white triangle) in CIE 1931 color space. d) Photographs of liquid crystal displays based on LEDs using CAO: Mn^{4+}, Be^{2+} and conventional LEDs using YAG.

3. Conclusion

A series of CAO:$0.002Mn^{4+}$, xBe^{2+} red phosphors were prepared by the high-temperature solid reaction. Upon excited by UV to blue light, the samples show red line emissions. Doping of Be^{2+} can effectively enhance the luminescence because the substitution of Be^{2+}-Mn^{4+} for Al^{3+}-Al^{3+} can compensate for the charge and suppress the self-reduction of Mn^{4+} to Mn^{2+}. Compared to Mn^{2+} and other divalent metal ions, Be^{2+} is closer to Al^{3+} in size and has the advantage of replacing Al^{3+} for change compensation, leading to remarkable luminescence enhancement with an internal quantum efficiency of 74.9% and external quantum efficiency of 56.3% with the optimal Be^{2+} concentration of 0.01. The backlight source based on CAO: Mn^{4+}, Be^{2+} achieves 110.1% NTSC and shows a more vibrant color.

4. Experimental Section

Sample Preparation: A series of $CaAl_{12}O_{19}$: $0.002Mn^{4+}$, xBe^{2+} ($x = 0$, 0.001, 0.01, 0.03, 0.05) and $CaAl_{12}O_{19}$: $0.002Mn^{4+}$, $0.01Re^{2+}$ (Re = Ba, Sr, Ca, Cd, Zn, Mg, Be) red phosphors were prepared by high-temperature solid reaction. $CaCO_3$ (AR), Al_2O_3 (4N), MnO_2 (4N), BeO (99%), $SrCO_3$ (99.95%), $BaCO_3$ (AR), ZnO (AR), CdO (AR), and MgO (AR) were weighed in molar ratio and ground in a mortar for 30 min. 5% H_3BO_3 (GR) was added as the flux. The milled samples were sintered at 1600 °C for 6 h. After natural cooling to room temperature, the samples were reground for subsequent characterization. In addition, CAO: $0.002Mn^{2+}$ was also prepared via 90% N_2 + 10% H_2 reduction at 1600 °C for 6 h.

Characterization: The patterns of XRD were given by a D8 Focus powder X-ray diffractometer (Bruker, Germany). The SEM and EDS were characterized by S4800 (Hitachi, Japan). The PL and PLE spectra were given by an FLS920 fluorescence spectrophotometer (Edinburgh Instrument, UK) excited by a 150 W Xenon lamp. Spectra@77 K were tested using a QEPro spectrophotometer (Ocean Optical, USA) with the excitation source of a Xenon lamp, and the temperature was controlled by a THMS600E cooling-heating platform (Linkam Scientific Instruments, UK). The fluorescence decay curves were recorded by a Tektronix digital oscilloscope and the excitation light was a Nd: YAG laser pumped with a pulsed laser output from Horizon OPO. A UV-3600 plus UV–vis-NIR spectrometer (Shimadzu, Japan) was used to record diffuse reflection spectra. XPS was measured by 250i (Thermo Fisher, USA) and EPR was measured by A300 (Bruker, Germany). Electroluminescence (EL) spectra were measured by the HAAS2000 photoelectric measuring system (350–2000 nm, EVERFINE, China). 4014 blue LED chips were used. The internal quantum efficiency (η_{IQE}) and external quantum efficiency (η_{EQE}) were measured by F7000 (Hitachi, Japan). Huawei Noval 7 was used for taking photos with IOS = 250 and s = 1/4. KSF and β-sialon were bought by Mitsubishi Chemical (Japan).

Supporting Information

Supporting Information is available from the Wiley Online Library or from the author.

ADVANCED
SCIENCE NEWS

www.advancedsciencenews.com

ADVANCED
OPTICAL
MATERIALS

www.advopticalmat.de

Conflict of Interest

The authors declare no conflict of interest.

Data Availability Statement

Research data are not shared.

Keywords

[1] Y. Li, Y. Yu, X. Zhong, C. Lu, D. Wu, S. Liao, Y. Huang, H. Zhang, *J. Lumin.* **2022**, *244*, 118728.

[2] Y. Yu, J. Qiang, D. Deng, T. Wang, X. Zhong, L. Wang, S. Liao, Y. Huang, *J. Lumin.* **2022**, *247*, 118885.

[3] T. T. Deng, E. H. Song, Y. Y. Zhou, L. Y. Wang, S. Ye, Q. Y. Zhang, *J. Mater. Chem. C* **2017**, *5*, 9588.

[4] S. Liang, M. Shang, H. Lian, K. Li, Y. Zhang, J. Lin, *J. Mater. Chem. C* **2016**, *4*, 6409.

[5] Y. Wei, H. Yang, Z. Gao, Y. Liu, G. Xing, P. Dang, A. A. Al Kheraif, G. Li, J. Lin, R.-S. Liu, *Adv. Sci.* **2020**, *7*, 1903060.

[6] H.-W. Chen, R.-D. Zhu, J. He, W. Duan, W. Hu, Y.-Q. Lu, M.-C. Li, S.-L. Lee, Y.-J. Dong, S.-T. Wu, *Light: Sci. Appl.* **2017**, *6*, e17043.

[7] M.-H. Fang, Z. Bao, W.-T. Huang, R.-S. Liu, *Chem. Rev.* **2022**, *122*, 11474.

[8] H. Ming, Y. Zhao, Y. Zhou, M. S. Molokeev, Y. Wang, S. Zhang, E. Song, S. Ye, Z. Xia, Q. Zhang, *Adv. Opt. Mater.* **2022**, *10*, 2102141.

[9] L. Huang, S. Lou, L. Cao, B. Liu, Y. Zhu, Y. Liu, C. Wang, J. Wang, *ACS Mater. Lett.* **2022**, *4*, 1716.

[10] J. Qiang, D. Deng, Y. Yu, T. Wang, X. Zhong, S. Liao, S. Li, *Appl. Surf. Sci.* **2022**, *604*, 154461.

[11] Z. W. Wang, Q. Qiao, H. P. Ji, X. F. Hao, J. S. Li, *Chin. J. Lumin* **2022**, *43*, 662.

[12] W. Zhang, M.-T. He, X.-S. Qiao, X. P. Fan, *Chin. J. Lumin.* **2021**, *42*, 1345.

[13] Y. Zhang, L. Luo, G. Chen, Y. Liu, R. Liu, X. Chen, *J. Rare Earths* **2020**, *38*, 1.

[14] B. Wang, H. Lin, J. Xu, H. Chen, Y. Wang, *ACS Appl. Mater. Interfaces* **2014**, *6*, 22905.

[15] W. Xu, D. Chen, S. Yuan, Y. Zhou, S. Li, *Chem. Eng. J.* **2017**, *317*, 854.

[16] Y. Zhong, S. Gai, M. Xia, S. Gu, Y. Zhang, X. Wu, J. Wang, N. Zhou, Z. Zhou, *Chem. Eng. J.* **2019**, *374*, 381.

[17] S. Fang, T. Lang, T. Han, J. Wang, J. Yang, S. Cao, L. Peng, B. Liu, A. N. Yakovlev, V. I. Korepanov, *Chem. Eng. J.* **2020**, *389*, 124297.

[18] K. Li, J. Du, D. Poelman, H. Vrielinck, D. Mara, R. Van Deun, *ACS Mater. Lett.* **2020**, *2*, 771.

[19] T. Senden, R. J. A. van Dijk-Moes, A. Meijerink, *Light: Sci. Appl.* **2018**, *7*, 8.

[20] M. H. Du, *J. Mater. Chem. C* **2014**, *2*, 2475.

[21] L. Kong, Y. Liu, L. Dong, L. Zhang, L. Qiao, W. Wang, H. You, *Dalton Trans.* **2020**, *49*, 1947.

[22] Z. Liu, M. Yuwen, J. Liu, C. Yu, T. Xuan, H. Li, *Ceram. Int.* **2017**, *43*, 5674.

[23] Y. Zhu, Z. Qiu, B. Ai, Y. Lin, W. Zhou, J. Zhang, L. Yu, Q. Mi, S. Lian, *J. Lumin.* **2018**, *201*, 314.

[24] S. Oguzlar, M. Z. Ongun, A. M. Deliormanli, *Opt. Mater.* **2021**, *117*, 111201.

[25] M. G. Brik, Y. X. Pan, G. K. Liu, *J. Alloys Compd.* **2011**, *509*, 1452.

[26] Y. X. Pan, G. K. Liu, *Opt. Lett.* **2008**, *33*, 1816.

[27] G. Fan, H. Zhang, D. Fan, R. Jiang, F. Ruan, N. Li, X. Su, *Dalton Trans.* **2021**, *50*, 13112.

[28] S. Ahn, H. Jung, D. Choo, T. Kim, J. Lee, J. Park, M. Kwon, *J. Electrochem. Soc.* **2010**, *157*, J238.

[29] C. Zhao, Y. Xu, L. Wang, X. Chen, W. Hu, Z. Dai, M. Hu, K. Liu, M. Shi, *J. Alloys Compd.* **2019**, *30*, 11419.

[30] T. Murata, T. Tanoue, M. Iwasaki, K. Morinaga, T. Hase, *J. Lumin.* **2005**, *114*, 207.

[31] Y. Wu, Y. Zhuang, R.-J. Xie, K. Ruan, X. Ouyang, *Dalton Trans.* **2020**, *49*, 3606.

[32] Y. Zheng, H. Zhang, H. Zhang, Z. Xia, Y. Liu, M. S. Molokeev, B. Lei, *J. Mater. Chem. C* **2018**, *6*, 4217.

[33] Y. Zhao, L. Shi, Y.-j. Han, H.-h. Li, Z.-x. Ji, Z.-w. Zhang, *Ceram. Int.* **2019**, *45*, 8265.

[34] Y. He, J. Liu, Y. Gao, L. Yan, F. Lv, F. Liu, L. Long, *J. Alloys Compd.* **2021**, *32*, 27513.

[35] W. Zhang, M. He, J. Jia, C. Liu, Q. Xu, X. Qiao, X. Fan, *J. Sol-Gel Sci. Techn.* **2022**, *104*, 434.

[36] G. Wang, Z. Li, W. Chen, *Xiyou Jinshu* **2011**, *35*, 520.

[37] M. Sagayama, U. Zafari, M. Subhoni, A. M. Srivastava, W. W. Beers, W. E. Cohen, M. G. Brik, T. Yamamoto, *ECS J. Solid State Sci. Technol.* **2021**, *10*, 076004.

[38] M. Brik, A. Srivastava, *J. Lumin.* **2013**, *133*, 69.

[39] H. Zhu, C. C. Lin, W. Luo, S. Shu, Z. Liu, Y. Liu, J. Kong, E. Ma, Y. Cao, R.-S. Liu, X. Chen, *Nat. Commun.* **2014**, *5*, 4312.

[40] S. Adachi, *J. Lumin.* **2020**, *218*, 116829.

[41] M. Brik, S. Camardello, A. Srivastava, *ECS J. Solid State Sci. Technol.* **2014**, *4*, R39.

[42] Y. Chen, J. Chen, J. Liang, J. He, Z.-Q. Liu, Y. Yin, *Chem. Mater.* **2020**, *32*, 9551.

[43] J. Xue, T. Hu, F. Li, F. Liu, H. M. Noh, B. R. Lee, B. C. Choi, S. H. Park, J. H. Jeong, P. Du, *Laser Photonics Rev.* **2023**, *17*, 2200832.

[44] R. Hoshino, S. Adachi, *J. Lumin.* **2015**, *162*, 63.

[45] L. Huang, Y. Zhu, X. Zhang, R. Zou, F. Pan, J. Wang, M. Wu, *Chem. Mater.* **2016**, *28*, 1495.

[46] H. F. Sijbom, R. Verstraete, J. J. Joos, D. Poelman, P. F. Smet, *Opt. Mater. Express* **2017**, *7*, 3332.

[47] C. Jiang, M. Peng, A. M. Srivastava, L. Li, M. G. Brik, *Inorg. Chem.* **2018**, *57*, 14705.

[48] F. Tang, Z. Su, H. Ye, W. Gao, X. Pan, S. Xu, *ACS Omega* **2018**, *3*, 13704.

[49] Z. W. Pei, Q. Su, J. Y. Zhang, *J. Alloys Compd.* **1993**, *198*, 51.

[50] Q. H. Zeng, Z. W. Pei, S. B. Wang, Q. Su, *J. Alloys Compd.* **1998**, *275*, 238.

[51] Y. Xu, L. Wang, B. Qu, D. Li, J. Lu, R. Zhou, *J. Am. Ceram. Soc.* **2019**, *102*, 2737.

[52] R. D. Shannon, *Acta Crystallogr.* **1976**, *A32*, 751.